Exploiting strained epitaxial germanium for scaling low-noise spin qubits at the micrometre scale

Stehouwer, Lucas E.A.; Yu, Cécile X.; van Straaten, Barnaby; Tosato, Alberto; John, Valentin; Degli Esposti, Davide; Elsayed, Asser; Costa, Davide; Oosterhout, Stefan D.; Hendrickx, Nico W.

DOI
10.1038/s41563-025-02276-w

Publication date
2025

Document Version
Final published version

Published in
Nature Materials

Citation (APA)
Stehouwer, L. E. A., Yu, C. X., van Straaten, B., Tosato, A., John, V., Degli Esposti, D., Elsayed, A., Costa, D., Oosterhout, S. D., Hendrickx, N. W., Veldhorst, M., Borsoi, F., & Scappucci, G. (2025). Exploiting strained epitaxial germanium for scaling low-noise spin qubits at the micrometre scale. *Nature Materials*, *24*(12), 1906-1912. https://doi.org/10.1038/s41563-025-02276-w

nature materials

Article

https://doi.org/10.1038/s41563-025-02276-w

Exploiting strained epitaxial germanium for scaling low-noise spin qubits at the micrometre scale

Received: 20 November 2024

Accepted: 28 May 2025

Lucas E. A. Stehouwer[1], **Cécile X. Yu**[1], **Barnaby van Straaten**[1], **Alberto Tosato**[1], **Valentin John**[1], **Davide Degli Esposti**[1], **Asser Elsayed**[1], **Davide Costa**[1], **Stefan D. Oosterhout**[2], **Nico W. Hendrickx**[1], **Menno Veldhorst**[1], **Francesco Borsoi**[1,3] & **Giordano Scappucci**[1,3] ✉

Disorder in the heterogeneous material stack of semiconductor spin qubit systems introduces noise that compromises quantum information processing, posing a challenge to coherently control large-scale quantum devices. Here we exploit low-disorder epitaxial, strained quantum wells in Ge/SiGe heterostructures grown on Ge wafers to comprehensively probe the noise properties of complex micrometre-scale devices, comprising quantum dots arranged in a two-dimensional array. We demonstrate an average low charge noise across different locations on the wafer, providing a benchmark for quantum confined holes. We then establish spin qubit control and extend our investigation from electrical to magnetic noise through spin echo measurements. Exploiting dynamical decoupling sequences, we quantify the power spectral density components arising from the hyperfine interaction with ^{73}Ge spinful isotopes and identify coherence modulations associated with the interaction with the ^{29}Si nuclear spin bath near the Ge quantum well, underscoring the need for full isotopic purification of the qubit host environment.

Recent progress with semiconductor spin qubits[1] has enabled proof-of-principle quantum processors[2–6] with error rates below the 1% threshold predicted to enable quantum error correction[7]. However, millions of highly coherent qubits need to be integrated to achieve a realistic quantum advantage[8]. One avenue to improve quantum performance at scale is by advancing material synthesis and fabrication processes to identify and mitigate the dominant noise sources[9]. Noise in semiconductor quantum systems has been predominantly studied in isolated components, such as single-charge transistors or individual spin qubits[10–17], with recent efforts exploring correlations[18] beyond nearest neighbours[19,20]. Operating large and highly connected spin qubit systems, in fact, requires a stringent level of electrostatic uniformity. This uniformity is challenged by the disorder introduced by complex semiconductor materials, gate stacks and interfaces, which collectively shape the potential landscape of coupled quantum dots.

Ge/SiGe heterostructures with exceptionally low disorder have recently been developed using Ge wafers as substrates for epitaxy, achieving an order-of-magnitude improvement in both dislocation density and two-dimensional (2D) hole gas mobility[21] compared to those grown on Si wafers[22] used for hole spin qubits[6,23–26]. This improvement is due to the reduced lattice mismatch between the substrate and the epitaxial, strained Ge quantum well, which is more than four times smaller for Ge wafers compared with Si wafers[27].

---

[1]QuTech and Kavli Institute of Nanoscience, Delft University of Technology, Delft, The Netherlands. [2]QuTech and Netherlands Organization for Applied Scientific Research (TNO), Delft, The Netherlands. [3]These authors contributed equally: Francesco Borsoi, Giordano Scappucci. ✉e-mail: g.scappucci@tudelft.nl

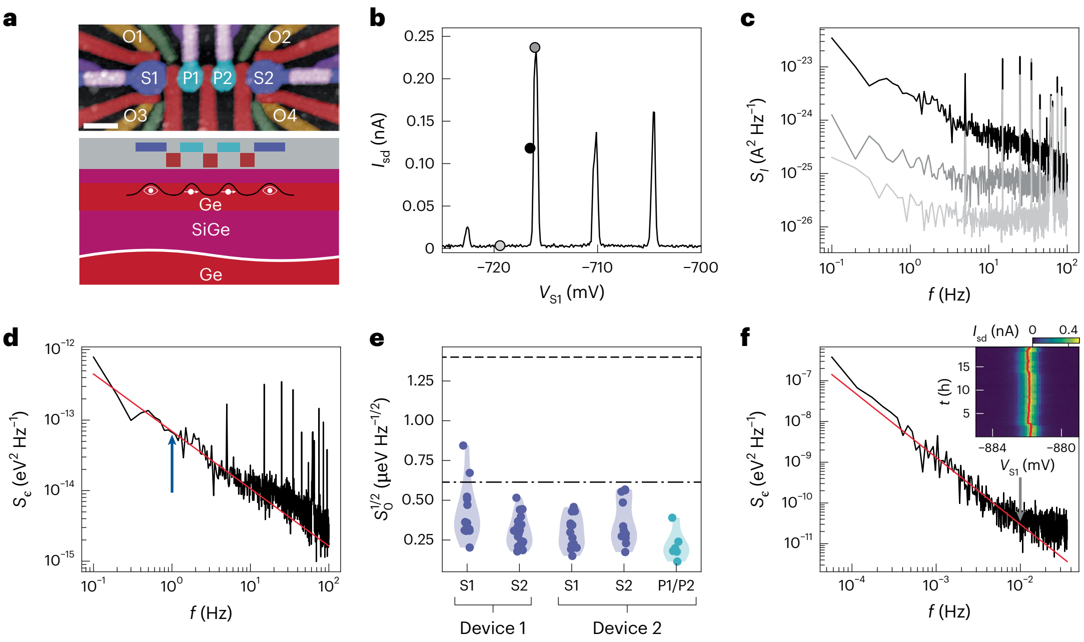

Fig. 1 | Charge noise in minimal quantum dot linear arrays. **a**, False-coloured atomic force microscopy image (top) of a device lithographically identical to the measured ones. The device comprises ohmic contacts (orange) and sensors (dark blue), plungers (light blue), barriers (red and green) and screening gates (purple). Scale bar,100 nm. The side view schematic (bottom) cutting through the sensor and plunger gates illustrates the confining electrostatic potential within the Ge/SiGe heterostructure grown on a Ge wafer. **b**, Source–drain current I_{sd} as a function of sensor voltage V_{S1} of device 2. Black, grey and light grey circles mark the flank, top and blockade regions, respectively, of a Coulomb peak for the measurement of current fluctuations. **c**, Corresponding current power spectral density S_I, with lines coloured to match positions in **b**. **d**, Representative charge noise power spectral density S_ϵ from the flank of the Coulomb peak at $V_{S1} = -716.2$ mV. The fit to S_0/f^α (red line) using a fitting range between 0.1 and 10 Hz yields a charge noise $S_0^{1/2}$ at 1 Hz (arrow) of 0.23(1) μeV $Hz^{-1/2}$. **e**, Distributions of $S_0^{1/2}$ from charge noise spectrum measurements as in **d** for different hole occupancies. Data points are presented as fitted values of $S_0^{1/2}$. The distributions of $S_0^{1/2}$ are represented by violin plots (shaded regions). Measurements are reported for the sensor and plunger gates from devices 1 and 2. As a comparison, dashed and dash-dotted lines are values from the literature (ref. 31 and ref. 13, respectively). **f**, Charge noise spectrum (device 2, sensor S1) extracted from ~18 h of Coulomb peak tracking (inset). The fit to S_0/f^α (red line) using a fitting range between 50 μHz and 10 mHz yields a charge noise of 5.5(9) μeV $Hz^{-1/2}$ at 10 mHz (grey arrow). The uncertainty is 1 s.d. from the fit. Inset: the red line tracks the voltage positions of the Coulomb peak; *t* is time.

Here we exploit such advancements in the semiconductor material stack to comprehensively study and benchmark the noise properties of holes in germanium. We probe simple systems, such as double quantum dots with sensors on the side, as well as more complex spin qubit devices, integrating ten quantum dots and four sensors in two dimensions. By employing a variety of tools, we assess statistically the noise power spectral density within the same device and across different devices on a wafer, measuring under different hole filling conditions. By adopting a single spin as a noise probe at three different qubit sites in a device, we distinguish and quantify the contribution of three noise mechanisms in natural germanium qubits: charge noise coupling via spin–orbit interaction and hyperfine interactions with the ^{73}Ge and ^{29}Si nuclear spins baths.

Charge noise in minimal quantum dot linear arrays

We characterize charge noise properties in small quantum dot linear arrays using the flank[12,15,16,28,29] and the Coulomb peak tracking (CPT)[12,17] methods. Here we focus on two nominally identical devices fabricated on the same high mobility Ge/SiGe heterostructure on a Ge wafer detailed in the literature[21]. The devices (Fig. 1a) comprise two inner quantum dots, under dot plunger gates labelled P1 and P2, and two charge sensors at the edges, under sensor plunger gates labelled S1 and S2. Figure 1b shows a representative Coulomb peak series from sensor S1 of device 2. Figure 1c illustrates the power spectral density S_I of the current fluctuations as a function of frequency *f*, probed at the top (grey), at the flank (black) and in the blockade region (light grey) of a Coulomb peak (Methods). Measurements performed at the flank yield the larger S_I, indicating that the noise floor of our set-up, probed with the relevant impedance of the load, is sufficiently low to measure the charge noise from the device[13].

By converting into an energy scale (Methods and Supplementary Fig. 1), we obtain in Fig. 1d the charge noise power spectral density S_ϵ, which we fit to the function S_0/f^α (red line), with $S_0^{1/2}$ being the charge noise amplitude at 1 Hz (blue arrow) and α the spectrum power law exponent. The approximate 1/*f* trend of the noise spectrum points towards an ensemble of two-level fluctuators with a wide range of activation energies[16,30]. However, we note that, under specific voltage configurations, we observe spectra that deviate from a simple 1/*f* trend (Supplementary Figs. 2–5), which could suggest a strong coupling to a single or a few dominating two-level fluctuators[16,30].

We build up statistics by iterating this protocol for different hole occupancies, various single-hole transistors and two different devices. We estimate an average charge noise value of $S_0^{1/2}$ of 0.3(1) μeV $Hz^{-1/2}$ and α of 0.9(2). Additionally, we probe the quantum dots under P1 and P2 in the multi-hole regime, obtaining comparable charge noise values (dark versus light blue dots in Fig. 1e). As highlighted in Fig. 1e, the average charge noise value compares favourably to previous reports. Our value is about two times lower compared with Ge quantum wells buried at the same depth of about 55 nm ($S_0^{1/2} = 0.6$ μeV $Hz^{-1/2}$; ref. 13) grown on a silicon substrate, and a factor of about five lower compared with shallow Ge quantum wells ($S_0^{1/2} = 1.4$ μeV $Hz^{-1/2}$; ref. 31) positioned 22 nm from the dielectric interface.

We extend the characterization towards lower frequencies by using the CPT method[12]. We track the Coulomb peak position in time (Fig. 1f, inset and Methods) and extract S_ϵ (Fig. 1f). We determine the

https://doi.org/10.1038/s41563-025-02276-w

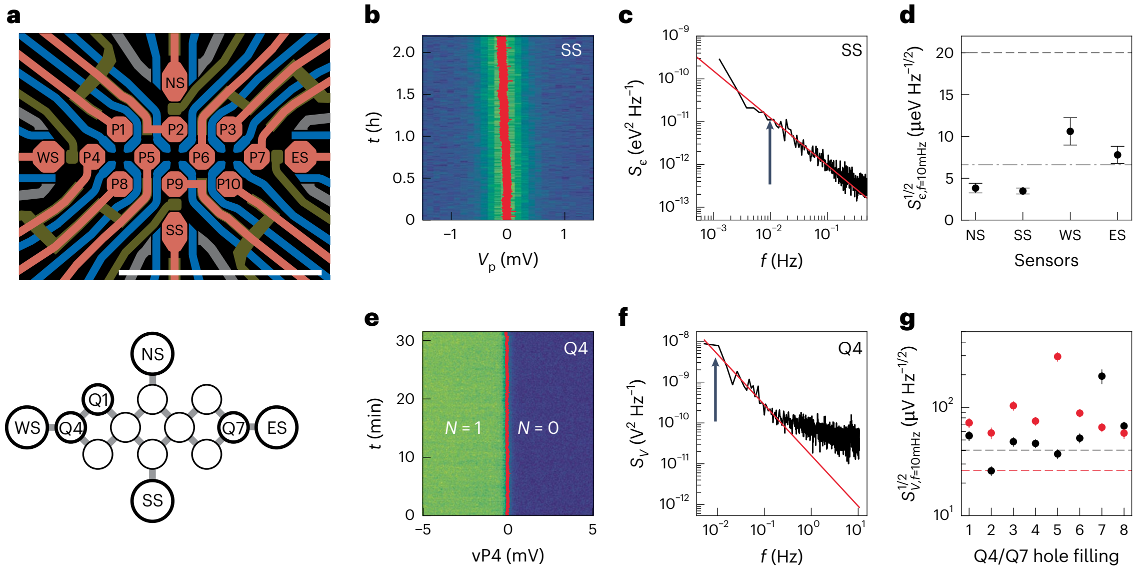

Fig. 2 | Charge noise in a micrometre-scale 2D quantum dot array. a, Schematic of the gate layout of the quantum dot array, hosting ten quantum dot qubits under plunger gates P1–P10, arranged in a 3–4–3 configuration. Quantum dots are read out by nearby charge sensors NS, ES, SS and WS. Scale bar, 1 μm. The interconnectivity of the array is shown below. The quantum dots investigated are shown as circles with a thick black line. **b**, Coulomb peak plunger voltage (V_p) tracking for the south sensor (SS) of the device. **c**, Charge noise power spectral density of the south sensor calculated from the Coulomb peak position fluctuations over time in **b**, with S_0/f^α fit between 1 and 100 mHz (red line) and arrow indicating the charge noise at a frequency of 10 mHz. **d**, Charge noise from the four sensors and benchmark to CPT experiment in Fig. 1f (dash-dotted line) and in the literature[17] (dashed line) at the same frequency (10 mHz). Data are the fitted values to $S^{1/2}_{\epsilon,f=10\text{mHz}}$, with error bars indicating the 1 s.d. of the fit. **e**, Repeated loading of the first hole on Q4 by sweeping the virtualized plunger gate (vP4). The red line estimates the $N = 0$ to $N = 1$ charge state transition position. **f**, Calculated voltage power spectral density from **e** with the extracted noise at 10 mHz (arrow) from the S_0/f^α fit between 10 and 200 mHz (red line). Uncertainties are 1 s.d. from the fitting procedure. **g**, Extracted voltage noise at 10 mHz for the first eight holes for Q4 (red) and Q7 (black). Data are represented as fitted values to $S^{1/2}_{V,f=10\text{mHz}}$, with error bars indicating 1 s.d. of the fit. The red (black) dashed line shows the voltage noise from sensor WS (ES), used to keep track of the charge state of quantum dot Q4 (Q7).

value at $f = 10$ mHz (grey arrow) by fitting the data to S_0/f^α and find a value of $S^{1/2}_{f=10\text{mHz}} = 5.5(9)$ μeV Hz$^{-1/2}$. When we extrapolate the $1/f^\alpha$ trend towards 1 Hz, we find $\alpha = 1.64(5)$ and $S_0^{1/2} = 0.26(1)$ μeV Hz$^{-1/2}$, in good agreement with the average noise of 0.3(1) μeV Hz$^{-1/2}$ from the flank method, confirming the reduced noise level in this heterostructure. The extracted α value of 1.64(5) from the CPT experiment differs from the one from the flank method ($\alpha = 0.9(3)$), possibly due to the presence of drift noise[16].

Charge noise in a micrometre-scale 2D quantum dot array

The improvement in the heterostructure disorder enables tuning of larger quantum dot arrays in two dimensions. The device shown in Fig. 2a comprises ten quantum dots arranged in a 3–4–3 configuration and with four radiofrequency (rf) charge sensors at the periphery[6]. We operate the array in the dense regime, with each quantum dot hosting either one, three or five holes. The outermost charge sensors are 1.5 μm apart, a distance that is comparable to the length scale of strain and compositional fluctuations of the heterostructure[21]. This spacing is therefore suitable for investigating the uniformity of noise on a large scale.

Figure 2b shows an example of a CPT measurement performed on the south sensor, SS (Supplementary Fig. 6 for the other sensors), with the corresponding charge noise power spectral density in Fig. 2c (Methods). This is fitted to S_0/f^α, from which we determine the charge noise values $S^{1/2}_{f=10\text{mHz}}$ at $f = 10$ mHz (black arrows in Fig. 2c), reported in Fig. 2d for the four sensors. The averaged noise across the sensors in this larger array is 6 μeV Hz$^{-1/2}$, comparable to the value of 5.5(9) μeV Hz$^{-1/2}$ measured in the smaller linear arrays (dash-dotted line in Fig. 2d). These findings suggest that the heterostructure maintains low noise levels both within the same device and across different devices. Moreover, a comparison with the best value (~20 μeV Hz$^{-1/2}$) for quantum dots defined on a Ge/SiGe heterostructure grown on a silicon substrate[17] (dashed line in Fig. 2d) shows a reduction in the noise amplitude by a factor of ≳3.

We focus on the stability of the inner quantum dots Q4 and Q7, and probe the susceptibility of noise to local perturbations of the electrostatic environment induced by different charge occupancy values[29]. As shown in Fig. 2e for quantum dot Q4, we repeatedly load the first hole into the quantum dot and track the transition voltage (red line; further analysis in Supplementary Fig. 7). We quantify the voltage power spectral density S_V (Fig. 2f) and estimate the voltage noise at a frequency of $f = 10$ mHz by fitting to S_0/f^α. In Fig. 2g we plot the voltage noise as a function of charge filling up to the eighth hole for quantum dots Q4 (black dots) and Q7 (red dots). We note that the voltage noise fluctuates largely between hole fillings, with average values at $f = 10$ mHz of 60(50) μV Hz$^{-1/2}$ and 90(70) μV Hz$^{-1/2}$ for quantum dots Q4 and Q7, respectively. On average, we obtain a value $\alpha = 1.0(3)$. As a comparison, we also measure the voltage noise of the corresponding charge sensors that were used to sense the charge transitions on the quantum dots (labelled WS for Q4, and ES for Q7) using CPT. We find that the noise of the sensors (black and red dashed lines for Q4 and Q7, respectively) is qualitatively comparable to the average noise of the quantum dots.

Charge and hyperfine noise in hole spin qubits

We exploit the spin degree of freedom as a sensitive noise probe of the local host environment and focus on the spin qubit pair confined in the double quantum dot system Q1–Q4. The associated charge stability diagram (Fig. 3a) reveals well-defined charge regions corresponding to different occupations centred around the $(n_{Q4}, n_{Q1}) = (1,3)$ charge state (with n_{Qi} indicating the number of carriers confined in quantum dot i) regime in which this pair is operated. A magnetic field is applied

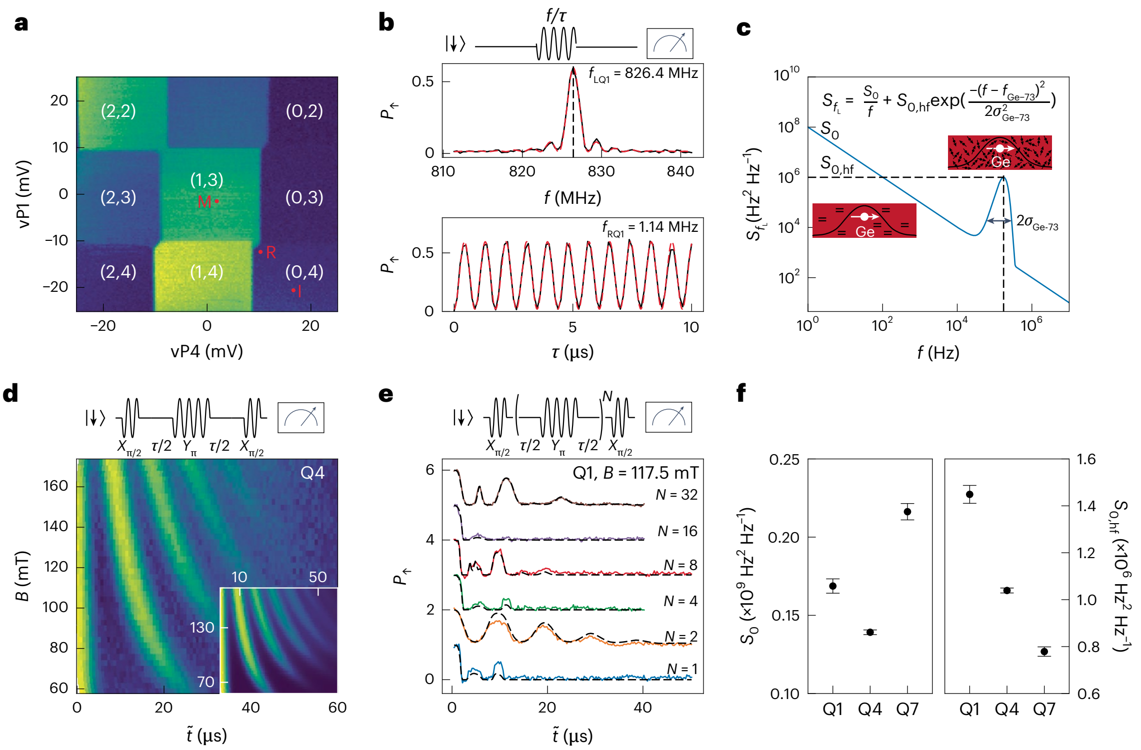

Fig. 3 | Charge and hyperfine noise characterization using spin echo measurement protocols. a, Charge stability diagram for qubit pair Q1–Q4 obtained by sweeping the two virtual plungers vP4 and vP1. Labels I, M and R indicate approximate virtual plunger gate voltages associated with the initialization, manipulation and read-out stages, respectively. **b**, Pulse sequence for Rabi experiments with drive at a frequency f and with duration τ (diagram). Exemplary Q1 electric dipole spin resonance spectroscopy (top) and Rabi oscillations (bottom) at $B = 117.5$ mT. $P_\uparrow$, spin-up probability. Larmor (f_{LQ1}) and Rabi (f_{RQ1}) frequencies are extracted by fitting the data, as discussed in the Methods. Data (best fit) are shown as a black (red dashed) trace. **c**, Model of the power spectral density affecting the hole spin qubits. The model consists of a $1/f$ contribution and a Gaussian peak arising from the hyperfine interaction with the ^{73}Ge non-zero nuclear spin. Insets: coupling of the hole spin qubit to two-level fluctuators (on the left) and to a bath of spinful nuclei (on the right). **d**, CPMG-1 experiment for a range of magnetic fields B measured on qubit Q4. Top: schematic of the pulse scheme. The time axis is defined as $\tilde{t} = \tau + t_\pi$, where the finite time of the Y_π pulse ($t_\pi = 1/(2f_R)$) is taken into account. We normalize the measured signal between 0 and 1 to facilitate the fitting procedure of the model of **c**. Inset: best fit to the normalized data using the noise model following the literature[26]. Data and fit show excellent agreement. **e**, Normalized CPMG-N pulse sequences (schematic on top) for $N = 1, 2, 4, 8, 16$ and 32 Y_π pulses for qubit Q1 at $B = 117.5$ mT. The black dashed line is the best fit from the noise model in **c** to the data. Each trace is shifted vertically by one unity for clarity. **f**, Extracted S_0 and $S_{0,hf}$ parameters for qubits Q1, Q4 and Q7 obtained from the data shown in **d**, **e** and Supplementary Fig. 8. Data are represented as fitted values to S_0 and $S_{0,hf}$, with error bars 1 s.d. from the fit.

to Zeeman split the spin states via a one-axis solenoid magnet that is nominally parallel to the sample plane.

We control the qubit pair by pulsing the voltages through the charge stability map. Starting at point I of Fig. 3a, we prepare a two-hole S(0,4) singlet state, and then ramp adiabatically to the centre of the (1,3) charge state (point M), preparing a |↑↓⟩ state with an unpaired spin in each quantum dot. We then perform qubit manipulation via electric dipole spin resonance, after which we read out the qubit state at point R using Pauli spin blockade. Parallel spin states (|↓↓⟩ and |↑↑⟩) are blocked and mapped into the (1,3) charge state, while antiparallel spin states (|↑↓⟩ and |↓↑⟩) are transferred into the (0,4) charge state, resulting in the so-called parity read-out[32–34] (Supplementary Fig. 8).

We proceed by calibrating the single-qubit gate parameters of each qubit to then exploit Carr–Purcell–Meiboom–Gill (CPMG) sequences to probe the power spectral density of the noise affecting the qubits[10,35–39]. Figure 3b illustrates electric dipole spin resonant control of Q1 through a microwave burst applied to the plunger P1 at a magnetic field of 117.5 mT for a varying driving frequency (top) and a varying driving time at the resonant condition (bottom). The Q1 and Q4 Larmor frequencies $f_{LQ1} = 826.4$ MHz and $f_{LQ4} = 954.5$ MHz map to effective g-factors of 0.503 and 0.577, respectively. By taking into account the pronounced anisotropy of the g-tensor of planar germanium quantum dots[40,41], we estimate a misalignment angle between the magnetic field direction and the substrate plane of ~3° (Methods), which has implications on the sources of noise that affect the qubit. Our hole spin qubits are, in fact, hosted in a Ge quantum well that has a natural 7.7 at.% relative abundance of the spinful ^{73}Ge isotope. The resulting fluctuating Overhauser field couples to the hole spin states via a hyperfine interaction of the Ising type that is highly anisotropic with the magnetic field direction[42,43].

Following the literature[26], we quantify the contribution to the qubit decoherence arising from both charge and hyperfine noise by modelling the spectral noise affecting the Larmor frequency (S_{f_L}) with a S_0/f contribution and a Gaussian peak at the precession frequency of the ^{73}Ge nuclear spins ($f_{Ge-73} = \gamma B$, with the expected gyromagnetic ratio $\gamma = 1.48$ MHz T^{-1} and B the magnetic field norm), as displayed in Fig. 3c.

We perform a series of CPMG-N experiments, consider the filter function associated with each sequence and estimate the noise spectral density by varying the number of refocusing Y_π pulses N (with Y_π corresponding to a rotation around the y axis of the Bloch sphere with an angle of π), the time in between two pulses and the magnetic field amplitude. We begin with the CPMG-1 experiment as a function of the magnetic field on qubit Q4. The resulting map in Fig. 3d manifests a clear collapse-and-revival pattern as a function of time, also known as hole spin echo envelope modulations[44,45], that is, dependent on the magnetic field. This phenomenon arises from the sharp noise component at $f_{Ge-73} \propto B$ that can be partially filtered only at times of n/f_{Ge-73} with n being an integer[26,46]. The inset of Fig. 3d illustrates the fit

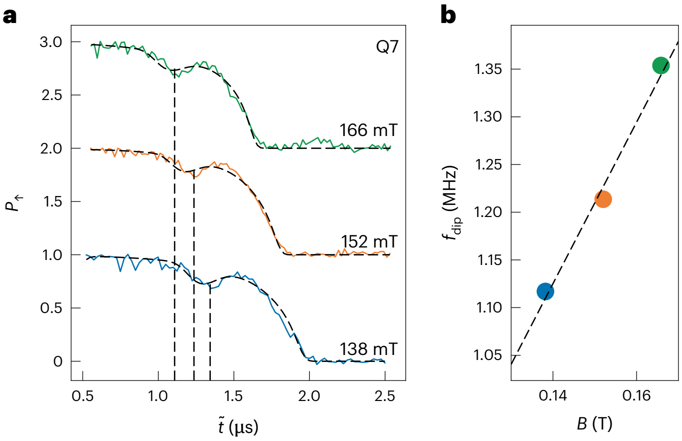

Fig. 4 | Influence of ^{29}Si nuclear spin on qubit coherence. a, Collapse and revival of the qubit Q7 spin state during a CPMG-64 measurement protocol for a magnetic field of 138 mT (blue), 152 mT (orange) and 166 mT (green). The dashed black line shows the best fit when taking into account a second Gaussian peak in the noise model from the ^{29}Si non-zero nuclear isotopes. Each trace is shifted upward by one unit for clarity. A dip in the coherence is observed between 1 μs and 1.5 μs and is attributed to the interaction with the ^{29}Si nuclear spins present in the SiGe barriers. **b**, Frequency f_{dip} converted from the time of the dip in **a**. From the linear fit we extract a gyromagnetic ratio of 8.6(9) MHz T^{-1}, which agrees with the expected 8.465 MHz T^{-1} for ^{29}Si.

to the data considering the noise model shown in Fig. 3c, which allows us to estimate the noise component at 1 Hz (S_0) and the amplitude of the hyperfine spectral peak ($S_{0,\text{hf}}$), together with its frequency spread ($\sigma_{\text{Ge-73}}$; Methods and Supplementary Fig. 9).

We extend the noise characterization using CPMG-N pulse sequences for $N = 1, 2, 4, 8, 16$ and 32 Y_π pulses. The results accompanied by fits at a fixed magnetic field of $B = 117.5$ mT are shown in Fig. 3e for qubit Q1, while measurements for $B = 138$ mT are shown in Supplementary Fig. 9. Using the same approach, we also probe qubit Q7 (Supplementary Fig. 9), which is located ~850 nm from Q4.

Figure 3f displays the extracted values of S_0 and $S_{0,\text{hf}}$ for the three qubits in a fixed magnetic field of $B = 117.5$ mT, resulting in an average value of S_0 equal to $0.17(3) \times 10^9$ Hz^2 Hz^{-1}. While nuclear spin effects could in principle also contribute to the low-frequency noise spectrum due to slow nuclear diffusion[47,48], we find it more plausible to associate the low-frequency component S_0/f to charge noise in the device. The extracted value of S_0, in fact, can be converted to a voltage noise level and compared with our findings on the electrical noise. We assume a spatially homogeneous distribution of uncorrelated fluctuators, and exploit knowledge of the g-factor susceptibility to voltage variations in all the surrounding gates[49]. Considering traps under the gates the most dominant, uncorrelated noise sources, we derive an effective voltage noise of $S_V^{1/2} = 12(1)\ \mu\text{V Hz}^{-1/2}$ (Methods). This is a twofold improvement with respect to the single qubit measured in the literature[26] for a germanium quantum well buried at a similar depth but grown on a silicon substrate. Moreover, assuming a ∝1/f framework, the value at 10 mHz (120(10) μV Hz$^{-1/2}$) lies within the range of what is detected from direct quantum dot measurements (80(60) μV Hz$^{-1/2}$), supporting our hypothesis.

The hyperfine noise values extracted from the three different qubits are in the same order of magnitude as in the literature[26] for qubits that are not operated on a hyperfine sweet spot (for example, not in a configuration with the magnetic field pointing in the substrate plane), with qubit-to-qubit variations that are amplified by the large anisotropy in the sensitivity to hyperfine noise. Exploiting the extracted noise parameters, we estimate an integrated hyperfine noise amplitude of $\sigma_f = 180(8)$ kHz, which sets an approximate upper bound for the hyperfine-limited dephasing time of $T_2^* = 1.25(5)$ μs, qualitatively similar to what was measured experimentally in the range of 1 μs to 2 μs (ref. 49; Methods). Performing a similar analysis on the low-frequency component, we predict a charge-noise-limited dephasing time of $T_2^* = 3.7(3)$ μs at 117.5 mT, and $T_2^* = 44(4)$ μs at 10 mT (refs. 6,15,50; Methods).

As, in practice, both noise components act on the qubits at the same time, we further use the model to validate the observed dependence of the Hahn decay time T_2^{H} (envelope decay) with the magnetic field, which, in the investigated magnetic field range, manifests a monotonic increase (shown for Q1 and Q4 in Supplementary Fig. 10). Our analysis suggests that for a magnetic field below ~150 mT, the dominant noise source is the hyperfine interaction with the ^{73}Ge bath. Coupling of the qubit to charge noise through spin–orbit interaction sets the boundary for T_2^{H} at a higher magnetic field, with a crossover point that exhibits an optimal T_2^{H} of ~40 μs.

Hyperfine interaction with ^{29}Si nuclei

Because the hole's wavefunction is electrostatically confined near the Ge/SiGe interface[51,52], the interaction with the spinful ^{29}Si nuclei in the barrier may potentially introduce an additional noise source affecting coherence. To isolate this possible decoherence mechanism, we perform a narrow-band noise measurement using a CPMG-64 sequence on qubit Q7 for three magnetic fields, as shown in Fig. 4a. In addition to the collapse of the coherence at ~2 μs due to the hyperfine interaction with the ^{73}Ge isotopes, we also observe a less pronounced dip between 1 μs and 1.5 μs. We extract the time associated with this dip in the $\tilde{t}$ axis ($\tilde{t}_{\text{dip}}$) and convert it into a frequency $f_{\text{dip}} = (2n-1)/2\tilde{t}_{\text{dip}}$ (with n indicating the harmonic). We then calculate f_{dip} for $n = 2$ for the three magnetic fields and use a linear fit to find a gyromagnetic ratio of 8.6(9) MHz T^{-1}, which agrees with the expected 8.465 MHz T^{-1} for ^{29}Si (Fig. 4b). We also find qualitative agreement when we expand our noise model with an additional Gaussian peak associated with the ^{29}Si nuclear spins (Methods), confirming that the qubit coherence is also influenced by the interaction with the ^{29}Si nuclear spin bath. From the fit of the three traces, we obtain the average parameters of $S_{0,\text{hf}}^{\text{Si-29}} = 9(1) \times 10^3$ Hz^2 Hz^{-1} and $\sigma_{\text{Si-29}} = 99(20)$ kHz, which results in an integrated hyperfine noise amplitude σ_f of 47(5) kHz and a ^{29}Si-limited dephasing time of $T_2^* = 4.8(7)$ μs (Methods).

Given the precision of the noise model to fit the data of Figs. 3d,e and 4a, we estimate an upper limit on the Hahn decay time T_2^{H} for the ideal case of perfect isotopic purification of both germanium and silicon (Methods). We obtain a T_2^{H} of around 0.4 ms at a small magnetic field of 10 mT, and of 36 μs for 117.5 mT, versus the experimentally detected measurements of 25 μs and 36 μs for Q1 and Q4, respectively (Supplementary Fig. 10). This shows the potential high gain in coherence when isotopically purifying the Ge quantum well, as well as the surrounding SiGe barrier layers, and operating the qubits at smaller magnetic fields.

Conclusions

We build a comprehensive understanding of noise in low-disorder Ge/SiGe heterostructures grown on Ge wafers by using a variety of tools applied to increasingly complex devices. In the multi-hole regime we observe consistently a low charge noise of 0.3(1) μeV Hz$^{-1/2}$ at 1 Hz. This value is a notable improvement over previous generations of Ge/SiGe heterostructure and sets a benchmark for quantum confined holes in semiconductors[13,17,31]. Previous studies of strained Ge/SiGe transistors on Si wafers[53,54], as well as Si/SiGe transistors[55] and quantum dots[15], have linked charge noise to electrically active dislocations originating below the quantum well. We speculate that charge noise in Ge/SiGe heterostructures grown on Ge wafers may be lower and more uniform than in those grown on Si wafers, due to the substantial reduced density of threading dislocations. However, when the voltage noise is probed as a function of hole occupancy, we observe large fluctuations associated with the specific hole filling.

We perform CPMG pulse sequences on three separate qubits and decouple the electrical noise from the magnetic noise by exploiting a theoretical model. We use the extracted parameters to quantify their contribution to decoherence in a range of magnetic fields and to make a prediction of the coherence time expected for a nuclear-spin-free heterostructure. Lastly, we use a CPMG-64 protocol to measure the modulation of coherence due to the spinful ^{29}Si isotope present in the SiGe barriers surrounding the Ge quantum well. This finding points towards a non-negligible overlap of the hole wavefunction with ^{29}Si, possibly related to Si–Ge mixing at the quantum well top Ge/SiGe interface, as observed by transmission electron microscopy in similar quantum wells[56].

Our study presents a framework for systematic charge and magnetic noise characterization in spin qubit devices and offers a starting point for future investigations of noise correlation to understand the challenges of error correction schemes in noisy intermediate-scale spin qubit devices. Furthermore, our findings motivate the optimization of the Ge/SiGe interface and the complete isotopic purification of the SiGe barrier layers surrounding the Ge quantum well[57].

Online content

Any methods, additional references, Nature Portfolio reporting summaries, source data, extended data, supplementary information, acknowledgements, peer review information; details of author contributions and competing interests; and statements of data and code availability are available at https://doi.org/10.1038/s41563-025-02276-w.

References

1. Burkard, G., Ladd, T. D., Pan, A., Nichol, J. M. & Petta, J. R. Semiconductor spin qubits. *Rev. Mod. Phys.* **95**, 025003 (2023).
2. Xue, X. et al. Quantum logic with spin qubits crossing the surface code threshold. *Nature* **601**, 343–347 (2022).
3. Mądzik, M. T. et al. Precision tomography of a three-qubit donor quantum processor in silicon. *Nature* **601**, 348–353 (2022).
4. Noiri, A. et al. Fast universal quantum gate above the fault-tolerance threshold in silicon. *Nature* **601**, 338–342 (2022).
5. Mills, A. R. et al. Two-qubit silicon quantum processor with operation fidelity exceeding 99%. *Sci. Adv.* **8**, 5130 (2022).
6. Wang, C.-A. et al. Operating semiconductor quantum processors with hopping spins. *Science* **385**, 447–452 (2024).
7. Fowler, A. G., Mariantoni, M., Martinis, J. M. & Cleland, A. N. Surface codes: towards practical large-scale quantum computation. *Phys. Rev. A* **86**, 032324 (2012).
8. Hoefler, T., Häner, T. & Troyer, M. Disentangling hype from practicality: on realistically achieving quantum advantage. *Commun. ACM* **66**, 82–87 (2023).
9. De Leon, N. P. et al. Materials challenges and opportunities for quantum computing hardware. *Science* **372**, abb2823 (2021).
10. Yoneda, J. et al. A quantum-dot spin qubit with coherence limited by charge noise and fidelity higher than 99.9%. *Nat. Nanotechnol.* **13**, 102–106 (2018).
11. Connors, E. J., Nelson, J., Qiao, H., Edge, L. F. & Nichol, J. M. Low-frequency charge noise in Si/SiGe quantum dots. *Phys. Rev. B* **100**, 165305 (2019).
12. Kranz, L. et al. Exploiting a single-crystal environment to minimize the charge noise on qubits in silicon. *Adv. Mater.* **32**, 2003361 (2020).
13. Lodari, M. et al. Low percolation density and charge noise with holes in germanium. *Mater. Quantum Technol.* **1**, 011002 (2021).
14. Zwerver, A. et al. Qubits made by advanced semiconductor manufacturing. *Nat. Electron.* **5**, 184–190 (2022).
15. Paquelet Wuetz, B. et al. Reducing charge noise in quantum dots by using thin silicon quantum wells. *Nat. Commun.* **14**, 1385 (2023).
16. Elsayed, A. et al. Low charge noise quantum dots with industrial CMOS manufacturing. *npj Quantum Inf.* **10**, 70 (2024).
17. Massai, L. et al. Impact of interface traps on charge noise and low-density transport properties in Ge/SiGe heterostructures. *Commun. Mater.* **5**, 151 (2024).
18. Yoneda, J. et al. Noise-correlation spectrum for a pair of spin qubits in silicon. *Nat. Phys.* **19**, 1793–1798 (2023).
19. Rojas-Arias, J. S. et al. Spatial noise correlations beyond nearest neighbors in ^{28}Si/Si-Ge spin qubits. *Phys. Rev. Appl.* **20**, 054024 (2023).
20. Donnelly, M.B. et al. Noise correlations in a 1D silicon spin qubit array. Preprint at https://doi.org/10.48550/arXiv.2405.03763 (2024).
21. Stehouwer, L. E. A. et al. Germanium wafers for strained quantum wells with low disorder. *Appl. Phys. Lett.* **123**, 092101 (2023).
22. Scappucci, G. et al. The germanium quantum information route. *Nat. Rev. Mater.* **6**, 926–943 (2021).
23. Hendrickx, N., Franke, D., Sammak, A., Scappucci, G. & Veldhorst, M. Fast two-qubit logic with holes in germanium. *Nature* **577**, 487–491 (2020).
24. Hendrickx, N. W. et al. A four-qubit germanium quantum processor. *Nature* **591**, 580–585 (2021).
25. Jirovec, D. et al. A singlet-triplet hole spin qubit in planar Ge. *Nat. Mater.* **20**, 1106–1112 (2021).
26. Hendrickx, N. et al. Sweet-spot operation of a germanium hole spin qubit with highly anisotropic noise sensitivity. *Nat. Mater.* **23**, 920–927 (2024).
27. Dismukes, J. P., Ekstrom, L. & Paff, R. J. Lattice parameter and density in germanium-silicon alloys. *J. Phys. Chem.* **68**, 3021–3027 (1964).
28. Connors, E. J., Nelson, J., Edge, L. F. & Nichol, J. M. Charge-noise spectroscopy of Si/SiGe quantum dots via dynamically-decoupled exchange oscillations. *Nat. Commun.* **13**, 940 (2022).
29. Spence, C. et al. Probing low-frequency charge noise in few-electron CMOS quantum dots. *Phys. Rev. Appl.* **19**, 044010 (2023).
30. Paladino, E., Galperin, Y., Falci, G. & Altshuler, B. 1/*f* noise: implications for solid-state quantum information. *Rev. Mod. Phys.* **86**, 361–418 (2014).
31. Hendrickx, N. W. et al. Gate-controlled quantum dots and superconductivity in planar germanium. *Nat. Commun.* **9**, 2835 (2018).
32. Seedhouse, A. E. et al. Pauli blockade in silicon quantum dots with spin-orbit control. *PRX Quantum* **2**, 010303 (2021).
33. Philips, S. G. J. et al. Universal control of a six-qubit quantum processor in silicon. *Nature* **609**, 919–924 (2022).
34. Takeda, K. et al. Rapid single-shot parity spin readout in a silicon double quantum dot with fidelity exceeding 99%. *npj Quantum Inf.* **10**, 22 (2024).
35. Meiboom, S. & Gill, D. Modified spin-echo method for measuring nuclear relaxation times. *Rev. Sci. Instrum.* **29**, 688–691 (1958).
36. Uhrig, G. S. Keeping a quantum bit alive by optimized π-pulse sequences. *Phys. Rev. Lett.* **98**, 100504 (2007).
37. Cywiński, Ł., Lutchyn, R. M., Nave, C. P. & Das Sarma, S. How to enhance dephasing time in superconducting qubits. *Phys. Rev. B* **77**, 174509 (2008).
38. Álvarez, G. A. & Suter, D. Measuring the spectrum of colored noise by dynamical decoupling. *Phys. Rev. Lett.* **107**, 230501 (2011).
39. Muhonen, J. T. et al. Storing quantum information for 30 seconds in a nanoelectronic device. *Nat. Nanotechnol.* **9**, 986–991 (2014).
40. Jirovec, D. et al. Dynamics of hole singlet-triplet qubits with large *g*-factor differences. *Phys. Rev. Lett.* **128**, 126803 (2022).
41. Van Bree, J. et al. Anisotropy of electron and hole *g* tensors of quantum dots: an intuitive picture based on spin-correlated orbital currents. *Phys. Rev. B* **93**, 035311 (2016).

42. Fischer, J., Coish, W. A., Bulaev, D. V. & Loss, D. Spin decoherence of a heavy hole coupled to nuclear spins in a quantum dot. *Phys. Rev. B* **78**, 155329 (2008).
43. Philippopoulos, P. *Hyperfine and Spin-Orbit Interactions in Semiconductor Nanostructures*. PhD thesis, McGill Univ. (2020).
44. Wang, X. J., Chesi, S. & Coish, W. A. Spin-echo dynamics of a heavy hole in a quantum dot. *Phys. Rev. Lett.* **109**, 237601 (2012).
45. Philippopoulos, P., Chesi, S., Salfi, J., Rogge, S. & Coish, W. A. Hole spin echo envelope modulations. *Phys. Rev. B* **100**, 125402 (2019).
46. Lawrie, W. I. L. *Spin Qubits in Silicon and Germanium*. PhD thesis, Delft Univ. of Technology (2022).
47. Chekhovich, E. A. et al. Nuclear spin effects in semiconductor quantum dots. *Nat. Mater.* **12**, 494–504 (2013).
48. Rojas-Arias, J. S. et al. The origins of noise in the Zeeman splitting of spin qubits in natural-silicon devices. Preprint at https://doi.org/10.48550/arXiv.2408.13707 (2024).
49. John, V. et al. A two-dimensional 10-qubit array in germanium with robust and localised qubit control. Preprint at https://doi.org/10.48550/arXiv.2412.16044 (2024).
50. Struck, T. et al. Low-frequency spin qubit energy splitting noise in highly purified ^{28}Si/SiGe. *npj Quantum Inf.* **6**, 40 (2020).
51. Terrazos, L. A. et al. Theory of hole-spin qubits in strained germanium quantum dots. *Phys. Rev. B* **103**, 125201 (2021).
52. Wang, C.-A. et al. Modeling of planar germanium hole qubits in electric and magnetic fields. *npj Quantum Inf.* **10**, 102 (2024).
53. Simoen, E. et al. Defect-related excess low-frequency noise in Ge-on-Si pMOSFETs. *IEEE Electron Device Lett.* **32**, 87–89 (2011).
54. Simoen, E. et al. Device-based threading dislocation assessment in germanium hetero-epitaxy. In *2019 34th Symposium on Microelectronics Technology and Devices (SBMicro)* 1–6 (IEEE, 2019).
55. Hua, W.-C., Lee, M. H., Chen, P. S., Tsai, M.-J. & Liu, C. W. Threading dislocation induced low frequency noise in strained-Si nMOSFETs. *IEEE Electron Device Lett.* **26**, 667–669 (2005).
56. Costa, D. et al. Reducing disorder in Ge quantum wells by using thick SiGe barriers. *Appl. Phys. Lett.* **125**, 222104 (2024).
57. Moutanabbir, O. et al. Nuclear spin depleted, isotopically enriched ^{70}Ge/^{28}Si^{70}Ge quantum wells. *Adv. Mater.* **36**, 2305703 (2024).

Methods

Heterostructure growth

The Ge/SiGe heterostructure material is grown using reduced-pressure chemical vapour deposition in an ASMI Epsilon 2000 reactor. Starting from a Ge wafer, a 2.5 µm strain-relaxed $\mathrm{Si}_{(1-x)}\mathrm{Ge}_x$ buffer is grown at a temperature of 800 °C with a final Ge concentration of $x = 0.83$ using three grading steps ($1 - x = 0.07, 0.13, 0.17$). We lower the growth temperature to 500 °C for the growth of the final 200 nm of the SiGe buffer layer, the 16 nm Ge quantum well, the 55 nm SiGe barrier layer and the sacrificial passivated Si cap layer. As measured in ref. 21, this heterostructure supports a 2D hole gas with a high maximum mobility of $3.4(1) \times 10^6\ \mathrm{cm}^2\,\mathrm{V}^{-1}\,\mathrm{s}^{-1}$ and a low percolation density of $1.22(3) \times 10^{10}\ \mathrm{cm}^{-2}$. The threading dislocation density is $6(1) \times 10^5\ \mathrm{cm}^{-2}$, nearly an order of magnitude lower than for the growth of Ge quantum wells with similar strain starting from a Si wafer.

Device fabrication

All devices are fabricated on the same Ge/SiGe heterostructure on a Ge wafer as that measured in ref. 21. The two linear array quantum dot devices are fabricated with multiple layers of Ti/Pd and platinum–germanosilicide (PtSiGe) ohmic contacts. These are defined by electron-beam lithography and created by thermally diffusing Pt at a temperature of 400 °C. A first layer of Ti/Pd (3/17 nm) barrier gates is separated from the heterostructure by a 7 nm $\mathrm{Al_2O_3}$ insulating oxide grown using atomic layer deposition. A second layer of Ti/Pd (3/37 nm) plunger gates is created and separated by 5 nm of $\mathrm{Al_2O_3}$ from the first layer of barrier gates. Details for the fabrication of the 3–4–3 device (2D quantum dot array) can be found in ref. 6.

Flank method electrical characterization of quantum dots

We cool multi-hole quantum dots defined underneath the charge sensor or plunger gates of a device in a Leiden cryogenic dilution refrigerator operating at a mixing chamber base temperature of 70 mK. To measure the charge noise using the flank method, we first set a source–drain bias (V_sd) of 0.1 mV across the device and subsequently tune the surrounding gates until we measure a current of 1 nA through the device. We define a multi-hole quantum dot underneath a sensor or plunger gate by fine tuning the barrier gates surrounding the gate of interest until we observe a spectrum of Coulomb peaks. We then measure the source–drain current I_sd on the left flank of the Coulomb peak where the slope $|\mathrm{d}I_\mathrm{sd}/\mathrm{d}V_\mathrm{sd}|$ of the Coulomb peak is the largest at a rate of 2 kHz for a duration of 100 s using a Keithley DMM6500 multimeter. To calculate the current power spectral density S_I, we first split each 100 s current trace into ten segments of 10 s each, and subsequently average over the current power spectral densities ($S_I = 1/N\sum_{i=1}^{N} S_I^i$) that we evaluate from each segment. For each Coulomb peak that we analyse, we convert the current power spectral density S_I into charge noise power spectral density S_ϵ using[15]

$$S_\epsilon = \frac{a^2 S_I}{|\mathrm{d}I_\mathrm{sd}/\mathrm{d}V_\mathrm{S}|^2}\,, \tag{1}$$

where V_S is the sensor voltage and a is the lever arm extracted from the analysis of the corresponding Coulomb diamond.

Coulomb peak tracking

On sensor 1 of device 2, we perform an ~18 h CPT experiment tracking the current I_sd through a quantum dot while continuously sweeping across the quantum dot using its plunger gate. For the four charge sensors of the 3–4–3 device, we track the reflected signal of each charge sensor for ~2 h when sweeping the sensor plunger gate voltage. We extract the position of the Coulomb peak by fitting each Coulomb peak to a hyperbolic secant function

$$y = \frac{a}{\cosh^2\left(b\left(x - x_0\right)\right)} + c\,, \tag{2}$$

where y reflects the measured signal, x is the sensor's plunger gate voltage, x_0 is the position for which the Coulomb peak is maximum and a, b and c are free fitting parameters. To calculate the voltage power spectral density S_V from the Coulomb peak fluctuations, we split them into ten equal segments and for each segment we calculate the voltage power spectral density from a Fourier transformation. We find the charge noise power spectral density S_ϵ (Fig. 3c) using the evaluated lever arm of each sensor and using

$$S_\epsilon = a^2 S_V. \tag{3}$$

Voltage noise estimation on single-hole quantum dots

To estimate the voltage noise of the quantum dots where we know the exact hole occupancy, we repeatedly load a hole into a dot by continuously sweeping the plunger gate voltage under which the quantum dot is defined. We keep track of the voltage for which a hole loads into a dot by fitting each voltage sweep to a sigmoid function given by

$$y = \frac{a}{1 + \exp\left(\frac{x - x_0}{\tau}\right)} + b\,, \tag{4}$$

where y reflects the measured signal, x_0 is the voltage for which a hole loads into a dot and a, b and τ are free fitting parameters. We split the voltage fluctuations into ten equal segments and calculate the voltage power spectral density S_V from a Fourier transformation. The final voltage power spectral density is calculated from the average of the ten segments. Because of the complexity in determining with accuracy the lever arm of the plunger gates to the quantum dots in this regime, we maintain the metric of the charge noise in voltage, rather than in energy.

Estimation of the relative out-of-plane angle between magnetic field and substrate

We consider the average effective g-factor $g_\mathrm{eff} = 0.58$ of the ten qubits[49] and assume in-plane principal g-tensor components of $g_x = -g_y = 0.04$ (ref. 6) and an out-of-plane component of $g_z = 11$ (ref. 26). Assuming the g-tensor axes follow the crystal directions, the effective g-factor can be written in terms of the out-of-plane angle θ and the principal components:

$$g_\mathrm{eff} = \sqrt{g_x^2\cos\theta^2 + g_z^2\sin\theta^2}. \tag{5}$$

By inverting the equation, we estimate the most plausible misalignment angle of $\theta = 3°$.

Extraction of Rabi and Larmor frequency

We extract the Larmor frequency f_L and Rabi frequency f_R by fitting the data with the following functions. For the Rabi frequency we use

$$P_\uparrow = A\sin(2\pi f_\mathrm{R}t + \phi)\exp(-t^2/\tau^2) + C\,, \tag{6}$$

where $P_\uparrow$ represents the measured up probability and t is the duration of the microwave burst. The Rabi frequency f_R, decay time τ, phase ϕ, amplitude A and offset C are free fitting parameters. The extraction of the Larmor frequency is done using

$$P_\uparrow = A\frac{f_\mathrm{R}^2}{f_\mathrm{R}^2 + \Delta^2}\sin^2\left(0.5t\sqrt{f_\mathrm{R}^2 + \Delta^2}\right) + C\,. \tag{7}$$

Here $\Delta = f - f_\mathrm{L}$ with f the probed frequency range during measurement; t, A, f_R, C and f_L are free fitting parameters.

Qubit noise model

Low-frequency and hyperfine noise affecting the qubits hosted in the natural Ge/SiGe heterostructure is modelled by[26]

$$S_{f_{\mathrm{L}}} = \frac{S_0}{f} + S_{0,\mathrm{hf}} \exp\left(\frac{-(f - f_{\mathrm{Ge-73}})^2}{2\sigma_{\mathrm{Ge-73}}^2}\right). \qquad (8)$$

Here, S_0 represents the low-frequency noise component at 1 Hz and $S_{0,\mathrm{hf}}$ represents the effective strength of the hyperfine noise acting on the qubit; $f_{\mathrm{Ge-73}} = \gamma_{\mathrm{Ge-73}} B$ is the precession frequency of ^{73}Ge determined by its gyromagnetic ratio $\gamma_{\mathrm{Ge-73}} = 1.48$ MHz T^{-1} and the magnetic field B; and $\sigma_{\mathrm{Ge-73}}$ represents the spread of the ^{73}Ge precession frequencies. We follow the same fitting procedure as outlined in the methods of ref. 26 to extract S_0, $S_{0,\mathrm{hf}}$ and $\sigma_{\mathrm{Ge-73}}$.

For the fitting of the data containing influence of the ^{29}Si nuclear spin, we expand equation (8) with a second Gaussian peak:

$$\begin{aligned} S_{f_{\mathrm{L}}} = \frac{S_0}{f} &+ S_{0,\mathrm{hf}}^{\mathrm{Ge-73}} \exp\left(\frac{-(f - f_{\mathrm{Ge-73}})^2}{2\sigma_{\mathrm{Ge-73}}^2}\right) \\ &+ S_{0,\mathrm{hf}}^{\mathrm{Si-29}} \exp\left(\frac{-(f - f_{\mathrm{Si-29}})^2}{2\sigma_{\mathrm{Si-29}}^2}\right). \end{aligned} \qquad (9)$$

The fitting procedure is split into a two-stage process, where we first use equation (8) to find $S_{0,\mathrm{hf}}^{\mathrm{Ge-73}}$ and $\sigma_{\mathrm{Ge-73}}$. We fix these parameters and then use equation (9) to find S_0, $S_{0,\mathrm{hf}}^{\mathrm{Si-29}}$ and $\sigma_{\mathrm{Si-29}}$. The precession frequencies of $f_{\mathrm{Ge-73}}$ and $f_{\mathrm{Si-29}}$ are also fixed.

Estimation of the hyperfine noise contribution

Using the average extracted parameters of $S_{0,\mathrm{hf}}^{\mathrm{Ge-73}} = 1.1(3) \times 10^6\ \mathrm{Hz}^2\ \mathrm{Hz}^{-1}$ and $\sigma_{\mathrm{Ge-73}} = 12(1)$ kHz that describe the modelled Gaussian peak in the power spectral density at the frequency $f_{\mathrm{Ge-73}}$, we estimate an integrated noise of the Larmor frequency fluctuations of

$$\sigma_f = \sqrt{\sqrt{2\pi} \times S_{0,\mathrm{hf}}^{\mathrm{Ge-73}} \sigma_{\mathrm{Ge-73}}} = 180(8)\ \mathrm{kHz}. \qquad (10)$$

This sets an approximate boundary for the hyperfine-limited dephasing time of $T_2^* = (\pi\sqrt{2}\sigma_f)^{-1} = 1.25(5)\ \mu\mathrm{s}$, qualitatively similar to what is measured experimentally, on the order of 1 μs to 2 μs (ref. 49).

We use the same procedure to assess the influence of the interaction with the ^{29}Si nuclei in the barrier to the Ge hole spin qubits. We consider the average parameters extracted from the fits in Fig. 4, $S_{0,\mathrm{hf}}^{\mathrm{Si-29}} = 9.0(8) \times 10^3\ \mathrm{Hz}^2\ \mathrm{Hz}^{-1}$ and $\sigma_{\mathrm{Si-29}} = 99(20)$ kHz, that lead to an integrated noise of $\sigma_f = 47(5)$ kHz and a ^{29}Si-limited $T_2^* = 4.8(4)\ \mu\mathrm{s}$.

Effective voltage noise and charge-noise-limited T_2^*

We assume a spatially homogeneous distribution of uncorrelated fluctuators, and exploit knowledge of the g-factor susceptibility to voltage variations in all the surrounding gates[49]. Considering traps under the gates the most dominant, uncorrelated noise sources, we can estimate the resulting overall g-factor susceptibility of the hole spin qubits as $\frac{\Delta g}{\Delta V} = \sqrt{\sum_i \left(\frac{\delta g}{\delta V_i}\right)^2} \approx 6.7 \times 10^{-4}\,\mathrm{mV}^{-1}$, with $\delta g/\delta V_i$ the susceptibility of the g-factor g to a voltage variation on each gate i (V_i) of the twelve barrier and ten plunger gates controlling the array. The associated Larmor qubit fluctuations result then into $\frac{\Delta f_{\mathrm{L}}}{\Delta V} = \frac{1}{h}\frac{\Delta g}{\Delta V}\mu_{\mathrm{B}} B$, where h is the Planck constant and μ_{B} is the Bohr magneton. For $B = 117.5$ mT the value of the fluctuations is ~1.1 MHz mV^{-1}. We can then derive an effective voltage power spectral density value at 1 Hz of

$$S_V = \frac{S_0}{\left(\frac{\Delta f_{\mathrm{L}}}{\Delta V}\right)^2} = 140(30)\ \mu\mathrm{V}^2\ \mathrm{Hz}^{-1} \qquad (11)$$

that results in an effective voltage noise of $S_V^{1/2} = 12(1)\ \mu\mathrm{V\ Hz}^{-1/2}$.

We evaluate the charge-noise-limited T_2^* using the extracted voltage noise amplitude of $S_V^{1/2} = 12(1)\ \mu\mathrm{V\ Hz}^{-1/2}$ at 1 Hz and the effective g-factor susceptibility of $\frac{\Delta g}{\Delta V} = 6.7 \times 10^{-4}\,\mathrm{mV}^{-1}$. The dephasing time T_2^* can be approximated in a quasi-static configuration by[6,15,50]

$$T_2^* = \frac{1}{\sqrt{2}\pi\Delta f}, \qquad (12)$$

with Δf the amplitude of the qubit frequency fluctuations due to a voltage noise with root mean square amplitude of $\Delta V_{\mathrm{r.m.s.}}$

$$\Delta f = \frac{\Delta g}{\Delta V}\Delta V_{\mathrm{r.m.s.}}. \qquad (13)$$

We compute $\Delta V_{\mathrm{r.m.s.}}$ over a period of time T assuming a power spectral density of S_V/f, and integrating the noise from low-frequency and high-frequency cut-off values, $f_{\mathrm{L}} = T^{-1}$ and f_{H}, respectively:

$$\Delta V_{\mathrm{r.m.s.}} = \sqrt{\int_{f_{\mathrm{L}}}^{f_{\mathrm{H}}} \frac{S_V}{f}\,\mathrm{d}f} = \sqrt{S_V \ln\frac{f_{\mathrm{H}}}{f_{\mathrm{L}}}}. \qquad (14)$$

By considering realistic values of $f_{\mathrm{L}} = 1$ mHz and $f_{\mathrm{H}} = 1$ MHz, we determine $\Delta V_{\mathrm{r.m.s.}} = 54(5)\ \mu\mathrm{V\ Hz}^{-1/2}$. We then distinguish two cases. For $B = 117.5$ mT, the resulting fluctuations lead to $\Delta f = 60(5)$ kHz and a charge-noise-limited dephasing time of $T_2^* = 3.7(3)\ \mu\mathrm{s}$. For a low magnetic field of 10 mT, we obtain an increased value of $T_2^* = 44(4)\ \mu\mathrm{s}$ due to the more than tenfold reduction in Δf.

Data availability

The datasets supporting the findings of this study are openly available via 4TU Research Data at https://doi.org/10.4121/33d97ca0-64be-496d-a440-218f376a9c4c.

Acknowledgements

We acknowledge D. H. A. J. ten Napel, P. Sberna, B. Morana and the team at the Else Kooi Laboratory of TU Delft for support with the ASMI Epsilon 2000 reactor that was used for the deposition of Ge/SiGe heterostructures. This work was supported by the Netherlands Organisation for Scientific Research (NWO/OCW), via the Frontiers of Nanoscience programme and the Open Competition Domain Science - M programme. We acknowledge support by the European Union through the IGNITE project with grant agreement no. 101069515 and the QLSI project with grant agreement no. 951852. F.B. acknowledges support from the Dutch Research Council (NWO) via the National Growth Fund programme Quantum Delta NL (grant no. NGF.1582.22.001). N.W.H. acknowledges support from the European Union through EIC Transition Grant GROOVE 101113173. A.T. acknowledges the research programme Materials for the Quantum Age (QuMat) for financial support. This programme (registration no. 024.005.006) is part of the Gravitation programme financed by the Dutch Ministry of Education, Culture and Science (OCW). This research was sponsored in part by the US Army Research Office (ARO) under award no. W911NF-23-1-0110. The views, conclusions and recommendations contained in this document are those of the authors and are not necessarily endorsed nor should they be interpreted as representing the official policies, either expressed or implied, of the ARO or the US Government. The US Government is authorized to reproduce and distribute reprints for government purposes notwithstanding any copyright notation herein. This research was sponsored in part by the Netherlands Ministry of Defence under award no. QuBits R23/009. The views, conclusions and recommendations contained in this document are those of the authors and are not necessarily endorsed nor should they be interpreted as representing the official policies, either expressed or implied, of the Netherlands Ministry of Defence. The Netherlands Ministry of Defence is authorized to reproduce and distribute reprints for government purposes notwithstanding any copyright notation herein.

Author contributions

L.E.A.S. grew the Ge/SiGe heterostructures, developed with input from G.S., D.D.E., A.T. and D.C.; A.T. fabricated quantum dot linear array

devices, along with D.C. and contributions from D.D.E. to process development. S.D.O. fabricated the 2D quantum dot array device. L.E.A.S. performed noise measurements of the quantum dot linear array devices, with help from A.E.; F.B., C.X.Y., B.v.S. and V.J. performed noise measurements of the 2D quantum dot array device. L.E.A.S. analysed the data with help from F.B. and N.W.H.; L.E.A.S., F.B. and G.S. wrote the paper with input from C.X.Y., B.v.S., N.W.H. and M.V.; G.S. and M.V. supervised the project, conceived by G.S.

Competing interests

N.W.H. is a founder, and M.V. and G.S. are founding advisors, of Groove Quantum BV, with N.W.H., M.V. and G.S. declaring equity interests. The other authors declare no competing interests.

Additional information

Supplementary information The online version contains supplementary material available at https://doi.org/10.1038/s41563-025-02276-w.

Correspondence and requests for materials should be addressed to Giordano Scappucci.

Peer review information *Nature Materials* thanks Danielle Holmes and the other, anonymous, reviewer(s) for their contribution to the peer review of this work.